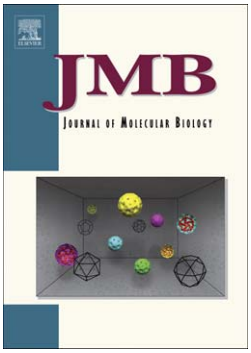

The C2B Domain Is The Primary Ca^{2+} Sensor In DOC2B: A Structural And Functional Analysis

Moshe Giladi, Lirin Michaely, Lior Almagor, Dana Bar-On, Tal Buki, Uri Ashery, Daniel Khananshvili, Joel A. Hirsch

PII: S0022-2836(13)00537-8
DOI: doi: 10.1016/j.jmb.2013.08.017
Reference: YJMBI 64204

To appear in: *Journal of Molecular Biology*

Received date: 28 June 2013
Revised date: 12 August 2013
Accepted date: 21 August 2013

Please cite this article as: Giladi, M., Michaely, L., Almagor, L., Bar-On, D., Buki, T., Ashery, U., Khananshvili, D. & Hirsch, J.A., The C2B Domain Is The Primary Ca^{2+} Sensor In DOC2B: A Structural And Functional Analysis, *Journal of Molecular Biology* (2013), doi: 10.1016/j.jmb.2013.08.017

The C2B Domain Is The Primary Ca^{2+} Sensor In DOC2B: A Structural And Functional Analysis

Moshe Giladi[a,*], Lirin Michaely[c,*], Lior Almagor[a,*], Dana Bar-On[c,d], Tal Buki[a], Uri Ashery[c,d], Daniel Khananshvili[a], and Joel A. Hirsch[b]

[a]Department of Physiology and Pharmacology, Sackler School of Medicine

[b]Department of Biochemistry and Molecular Biology, Institute of Structural Biology, George S. Wise Faculty of Life Sciences

[c]Department of Neurobiology, George S. Wise Faculty of Life Sciences

[d]Sagol School of Neuroscience

Tel-Aviv University

Ramat-Aviv 69978

Israel

* These authors contributed equally.

Correspondence to: Joel A. Hirsch, Department of Biochemistry and Molecular Biology, Faculty of Life Sciences, and Daniel Khananshvili, Department of Physiology and Pharmacology, Sackler School of Medicine, Tel-Aviv University, Ramat-Aviv, Tel-Aviv 69978, Israel. Tel/Fax: 972-3-640-7931; E-mail: jhirsch@post.tau.ac.il or dhanan@post.tau.ac.il

Abstract

DOC2B (double-C_2 domain) protein is thought to be a high-affinity Ca^{2+} sensor for spontaneous and asynchronous neurotransmitter release. To elucidate the molecular features underlying its physiological role, we determined the crystal structures of its isolated C2A and C2B domains and examined their Ca^{2+} binding properties. We further characterized the solution structure of the tandem domains (C2AB) using small-angle X-ray scattering. In parallel, we tested structure-function correlates with live cell imaging tools. We found that despite striking structural similarity, C2B binds Ca^{2+} with considerably higher affinity than C2A. The C2AB solution structure is best modeled as two domains with a highly flexible orientation and no difference in the presence or absence of Ca^{2+}. In addition, kinetic studies of C2AB demonstrate that, in the presence of unilamellar vesicles, Ca^{2+} binding is stabilized, as reflected by the ~10 fold slower rate of Ca^{2+} dissociation than in the absence of vesicles. In cells, isolated C2B translocates to the PM with an EC_{50} of 400 nM while the C2A does not translocate at submicromolar Ca^{2+} concentrations, supporting the biochemical observations. Nevertheless, C2AB translocates to the plasma membrane with a ~ 2 fold lower EC_{50} and to a greater extent than C2B. Our results, together with previous studies, reveal that the C2B is the primary Ca^{2+} sensing unit in DOC2B, whereas C2A enhances the interaction of C2AB with the plasma membrane.

Keywords: C_2 domain, exocytosis, synaptic transmission, Small-angle X-ray scattering, X-ray crystallography

Abbreviations

ASA – accessible surface area
DOC – double C_2
Dmax – maximum inter-atomic dimension
EOM – ensemble optimization method
MD – molecular dynamics
PC- phosphatidylcholine
PDDF – paired distance distribution function
PL – phospholipid
PM – plasma membrane
PS- phosphatidylserine
PE- phosphatidylethanolamine
Rg – radius of gyration
SAXS – small angle x-ray scattering
ULV – unilamellar vescicle

Introduction

Exocytosis is a central process in cell-cell communication in which intracellular vesicles fuse with the plasma membrane (PM), thus releasing their content to the extracellular milieu. This process, as well as other processes in the synapse depends on Ca^{2+}, which interacts with Ca^{2+}-binding domains of specific regulatory proteins, leading to a series of Ca^{2+}dependent processes in the synapse. [1; 2; 3]

One of most prominent Ca^{2+}-binding domains is the C_2 domain. Structurally, C_2 domains consist of ~130 residues organized in a sandwich of two four-stranded anti-parallel β-sheets. Ca^{2+} binds to the Ca^{2+}-binding region, comprise of two inter-strand loops via five conserved acidic residues. [4; 5] Many C_2 domains also bind soluble NSF attachment receptor (SNARE) proteins, key proteins in vesicle fusion, and anionic phospholipids (PLs), including phosphatidylserine (PS) and phosphatidylinositides, in a Ca^{2+} dependent manner. [6; 7; 8; 9; 10; 11] In turn, the binding of PLs increases the affinity of the C_2 domains for Ca^{2+}. [8; 12; 13; 14; 15; 16] Ca^{2+} binding induces large electrostatic changes, leading to membrane binding, rather than large conformational changes in the C_2 domain itself. [17; 18; 19] However, limited data is available regarding the effect of Ca^{2+} on interdomain motions i.e. between C_2 domains in the many proteins containing multiple C_2 domains. [20; 21]

Despite structural similarities, different C_2 domains exhibit different properties allowing them to take part in different forms of exocytosis such as synchronous, asynchronous, and spontaneous, as well as in other synaptic processes. For instance, the two sequential C_2 domains of synaptotagmin (syt) 1,2,9 exhibit fast response kinetics with relatively low Ca^{2+} affinity, imparting these proteins with the ability to function as the primary Ca^{2+} sensors for synchronous release. [22] In contrast, the two tandem C_2 domains of double C_2 (DOC2) domain proteins, DOC2A and DOC2B, exhibit high Ca^{2+} affinity and slower response kinetics. [23; 24] FRET experiments showed bi-phasic dissociation of DOC2B tandem C_2 domains (termed C2AB) from unilamellar vesicles (ULVs) upon Ca^{2+} removal, with the slower rate constant matching the time course of asynchronous release. [24] Indeed, DOC2A and DOC2B have been implicated in asynchronous and spontaneous release. [6; 24; 25]

In addition, despite striking similarities, C_2 domains are highly versatile from a biochemical standpoint. For example, in syt1 the C2A binds three Ca^{2+} ions with K_d values of 0.075, 0.5 and >1 mM, and its C2B binds two Ca^{2+} ions with affinity of approximately 0.3-0.6 mM. [26; 27] In

Rabphilin3A, which shares the highest known homology (>80%) with the DOC2B C_2 domains, both C_2 domains bind two Ca^{2+} ions; the C2A domain with affinity of 1.1 mM, [15] and the C2B domain with affinity in the μM range. [16; 28] However, to date, the intrinsic Ca^{2+} binding properties of the DOC2B C_2 domains have not been thoroughly studied, although they were shown to bind PLs and SNAREs in a Ca^{2+}-dependent manner. [6; 7]

Here, we investigate the biochemical and structural properties of the DOC2B C_2-domains. To elucidate the effect of Ca^{2+} binding and its coordination scheme, we determined the crystal structures of C2A in its Ca^{2+} bound and free forms at 2.0 Å resolution and the crystal structure of C2B in its Ca^{2+} bound form at 1.26 Å resolution. To explore the effect of Ca^{2+} on interdomain dynamics, we investigated C2AB in solution using small angle X-ray scattering (SAXS). We further examined $^{45}Ca^{2+}$ binding to isolated C2A and C2B domains and Ca^{2+}dissociation kinetics from C2AB in the absence and presence of PLs. Finally, we performed Ca^{2+} imaging in PC12 cells expressing each of the domains and calculated the Ca^{2+}-dependent EC_{50} values required for PM translocation of specific constructs. Taken together, our studies reveal that despite the striking similarities in Ca^{2+} binding sites, the two domains have distinct functions: C2B operates as the primary Ca^{2+} sensor of DOC2B, whereas C2A has a stabilizing effect on C2AB interaction with the membrane. Moreover, Ca^{2+} binding to the primary sensor induces large electrostatic changes with very small, if any, changes in intra and inter-domain conformations, whereas the two-domain orientations are highly flexible even in the presence of Ca^{2+}. PLs dramatically decelerate Ca^{2+} dissociation, suggesting that Ca^{2+}-dissociation may precede the detachment of DOC2B from the PM.

Results

Structural overview – C2A crystals diffracted to 2.0 Å resolution and contained four monomers in the asymmetric unit (ASU), of which two had an electron density break in the Ca^{2+}-binding region, one had two bound Ca^{2+} ions (with partial occupancies) and one had no ions bound. C2B crystallized as a monomer in the asymmetric unit, with two bound Ca^{2+} ions, and diffracted to 1.26 Å resolution. Crystallographic data collection and refinement statistics are summarized in Table 1. Both domains share overall fold of type I C_2 topology, [4] as described (Figure 1A). However, the C2B domain contains an additional relatively long α-helix between strands 7 and 8, similarly to the rabphilin C2B

domain. [28] Ca^{2+} bound C2A and C2B can be superimposed with a r.m.s.d (root mean square deviation) of 0.98 Å. The Ca^{2+} bound and apo forms of C2A are nearly identical, with a r.m.s.d of 0.40 Å, the differences arising mainly from different conformations of the Ca^{2+} binding loops (Figure 1A and Figure 3A-B). A model of apo C2B was obtained using molecular dynamics, based on the Ca^{2+} crystal structure, in order to assess the electrostatic effects of Ca^{2+} binding. Comparing the electrostatic potentials of the Ca^{2+} bound and apo forms of both domains (Figure 1B), Ca^{2+} binding results in a negative-to-positive shift of the potential at the Ca^{2+} binding site vicinity, favoring interactions with the negatively charged phospholipid bilayer, as proposed previously for other family members. [17]

Solution conformation of C2AB – In order to study possible interactions between the C_2 domains in the context of C2AB and to detect Ca^{2+} induced conformational changes, we utilized SAXS (Figure 2), a method for low resolution structural analysis in solution. The radius of gyration (R_g) and I(0) were derived from the Guinier region ($qR_g < 1.3$) and are very similar, indicating that Ca^{2+} binding does not induce global conformational changes (Table 2). The paired distance distribution functions (PDDF) of the apo and Ca^{2+} bound forms are also nearly identical, with D_{max} = 80 ± 8 Å and D_{max} = 83 ± 8 Å, respectively (Figure 2D, Table 2). Finally, the calculated Porod volumes are similar and consistent with monomeric C2AB (Table 2).

For determination of the domains' orientation in the C2AB tandem, two approaches were used. First, the isolated domain crystal structures were used for rigid-body fitting using SASREF. [29] Although the data is well fit in the low angles, a systematic deviation is observed at higher angles (Figure 2A). In attempt to better model the data, we used the ensemble optimization method (EOM) (Figure 2B).[30] In this method, an ensemble containing 20 models is chosen from a 10,000 models pool. The pool is generated by random construction of the domains linker (following only stereochemical restrains), thus containing a variety of possible orientations. This approach resulted in an excellent fit for the entire scattering range. The selected ensembles are very similar for both the apo and Ca^{2+} bound data (Figure 2C), again suggesting that Ca^{2+} does not induce global conformational transitions. Interestingly, the distributions are bi-modal and span the entire range of both possible D_{max} and R_g values (Figure 2C,E). Thus, the tandem is highly flexible, but some orientations are preferred

and the arrangement is not completely random. This analysis also revealed that the D_{max} of a small fraction of the population can extend to > 120 Å (Figure 2C).

Ca^{2+} binding sites – Although both domains were crystallized at the same Ca^{2+} concentration (200 μM), C2B crystallized in the Ca^{2+} bound form while only one C2A monomer out of four in the asymmetric unit was Ca^{2+} bound. Furthermore, the bound ions had only partial occupancy (0.32 and 0.39). Nevertheless, the Ca^{2+} binding stereochemistry of both domains is strikingly similar.

In C2A (Figure 3A), one Ca^{2+} ion is coordinated by the backbone carbonyl of M156 and carboxyl oxygens of D157, D218, D220 and E226. The second ion is coordinated by the backbone carbonyl of E219 and carboxyl oxygens of D157, D163, D218 and D220. Thus, both ions share similar overall coordination, with one carboxyl oxygen and 5 carboxyl oxygen atoms, in agreement with the similar occupancy for both ions.

In C2B (Figure 3C), one Ca^{2+} ion is coordinated by the backbone carbonyl of M296 and carboxyl oxygen of D297, D357, D359 and D365. The second ion is coordinated by the backbone carbonyl of Y358 and carboxyl oxygens of D297, D303, D357 and D359 and a water molecule. Again, both ions share similar overall coordination, with one carboxyl oxygen and five carboxyl oxygen atoms. Notably, the ion coordination in both domains is essentially the same as that described for the C_2 domains of rabphilin-3A.[14; 28] We observe a dyad symmetry in the C2B Ca^{2+} binding site, where D303 is related to D365 and D297 is related to D359 and D357 lies on the dyad axis.

Ca^{2+} binding to isolated C_2 domains – The different Ca^{2+} binding occupancies in the crystal suggested that the domains differ in their Ca^{2+} binding affinity, despite having very similar binding sites. In order to test this possibility, $^{45}Ca^{2+}$-binding assays were performed to evaluate the affinity and stoichiometry of Ca^{2+} binding (Figure 3D). Both C2B and the tandem C2AB bind two Ca^{2+} ions (capacity = 2.37 ± 0.11 and 1.94 ± 0.02, respectively) in a highly cooperative fashion (n_H = 1.65 ± 0.03 and 1.46 ± 0.01, respectively) with nearly identical K_d values (9.6 ± 0.1 and 9.84 ± 0.3 μM, respectively) (Figure 3D). This result suggests that in the tandem C2AB, C2A does not bind Ca^{2+}. Indeed, Ca^{2+} binding to C2A could not be detected up to $[Ca^{2+}]_{free}$ = 100 μM (Figure 3D). For C2A, the free and total $[Ca^{2+}]$ are nearly identical, resulting in "negative" occupancy of some data points due to the small experimental error (~ 2%). These results are in line with the structural data, since 200 μM $[Ca^{2+}]$ gave only partial

occupancy in one out of four C2A molecules in the crystal (Figure 1A). The measured K_d values for both C2A and C2B domains are significantly higher than the EC_{50} observed for DOC2B in cellular systems (< 1 μM), suggesting that, binding of phospholipids modifies the domains' intrinsic affinity, similar to other C_2 proteins. [12; 14]

Membrane binding sites – A previous study suggested that the membrane penetrating residues are H158 and F222 in C2A and A298 and I360 in C2B. [6] Another study suggested that N159 participates in membrane penetration rather than H158. [7] Utilizing the crystal structures of both C2A forms, apo and Ca^{2+} bound, we assessed the effect of Ca^{2+} on the membrane penetrating residues (Figure 4) by examining B-factors, a measure of a residues' mobility, and accessible surface area (ASA). Upon Ca^{2+} binding, the B-factor of H158 increases from 27.5 ± 2.1 $Å^2$ to 56.3 ± 4.6 $Å^2$, the B-factor of N159 increases from 24.4 ± 2.6 $Å^2$ to 54.3 ± 2.8 $Å^2$ and that of F222 decreases from 74.8 ± 2.1 $Å^2$ to 38.6 ± 2.4 $Å^2$. The accessible surface area (ASA) of H158 increases from 75.0 $Å^2$ to 194.9 $Å^2$, however the ASA of N159 decreases from 128.9 $Å^2$ to 90.0 $Å^2$ and that of F222 slightly increases from 204.6 $Å^2$ to 206.5 $Å^2$. Both the greater mobility and surface area for H158 suggest that it may be the residue that penetrates the PM while N159 is a less likely candidate as its ASA actually decreases upon Ca^{2+} binding. Consistent with such a conclusion, superposition with the structures of syt1 C2A (Figure 4C) shows that in the Ca^{2+} bound form, H158 and F222 of DOC2B occupy positions similar to those of M173 and F234, the membrane penetrating residues of syt1. [31; 32] As the apo C2B was obtained by molecular dynamics and not X-ray crystallography, we cannot compare the B-factors between the apo and Ca^{2+} bound forms. However, ASA analysis shows that the ASA of A298 increases from 101.2 $Å^2$ to 120 $Å^2$ (similarly to H158), while the ASA of I360 only changes slightly from 134.8 $Å^2$ to 134.4 $Å^2$ (similarly to F222), upon Ca^{2+} binding.

Ca^{2+} dissociation kinetics from C2AB – It was recently shown that the dissociation kinetics of C2AB from liposomes upon Ca^{2+} removal closely matched those of asynchronous transmitter release. [24] However, it remains unknown what is the rate-limiting step of this process, i.e., dissociation of DOC2B from the phospholipids or Ca^{2+} from DOC2B. In order to monitor the Ca^{2+} dissociation kinetics, we used the fluorescent indicator Quin-2, which exhibits a rise in fluorescence intensity upon Ca^{2+} binding (Figure 5A). Upon mixing, $[Ca^{2+}]_{free}$ drops during the dead time as it rapidly binds to

Quin-2, thereby driving Ca^{2+} dissociation from the protein, monitored as rise in Quin-2 fluorescence. Since Ca^{2+} binding to Quin-2 is nearly a diffusion-controlled reaction, the fluorescence rise kinetics reliably reflects those of Ca^{2+} dissociation from the examined protein. [33] In the absence of vesicles, Ca^{2+} dissociates from C2AB with a rate constant of 264.5 ± 17.7 s^{-1} (n=6) (Figure 5A-B). In contrast, in the presence of ULVs, Ca^{2+} dissociates from C2AB with a rate constant of 36.5 ± 0.7 s^{-1} (n = 6) (Figure 5A-B).

The C2B domain acts as the primary Ca^{2+} binding motif in cells – Our data thus far implicate C2B as the primary Ca^{2+} binding domain of DOC2B. To further test the in vitro findings, we performed live cell Ca^{2+} imaging and examined the correlation between Ca^{2+} elevation and the translocation to the PM of various DOC2B domains. PC12 cells over-expressing either full-length DOC2B, tandem C2AB, isolated C2A or isolated C2B fused to eGFP were pre-loaded with the Ca^{2+} indicator Fura-4F AM. We have previously used this approach to characterize the EC_{50} of DOC2A and DOC2B. [1; 23] During the experiment, cells were repeatedly depolarized by a high potassium (100 mM) containing solution, and monitored for their Ca^{2+} levels and translocation status (Figure 6A-B). Ca^{2+} EC_{50} values required for plasma-membrane (PM) translocation and the Hill slopes were calculated for the different constructs (Figure 6B-C). Consistent with our biochemical results, C2B was more sensitive to Ca^{2+} than C2A and translocated to the PM at submicromolar Ca^{2+} concentrations (EC_{50} = 0.5 ± 0.06 μM; Figure 6A-C). C2A did not translocate following physiological Ca^{2+} elevation (to a level of 1-2 μM) and only if ionophore was applied to the cells did the C2A of DOC2B translocate to the PM (Figure 6A, lower panel). The tandem C2AB fragment demonstrated two-fold higher Ca^{2+} sensitivity (EC_{50} = 0.24 ± 0.02 μM, Figure 6B-D) than C2B. In addition, C2B translocated to a lesser extent then both the full length protein and the tandem C2AB (Figure 6B). These results suggest that although C2A alone does not translocate at submicromolar Ca^{2+} concentrations, it can enhance and stabilize the translocation of C2B, acting in a concerted fashion in the context of the native protein. The full length protein exhibits Ca^{2+} sensitivity similar to that of the C2AB tandem (EC_{50} = 0.35 ± 0.03 μM; Figure 6B). Importantly, C2B, C2AB and DOC2B show similar Hill coefficients (Figure 6C), consistent with cooperative binding of ~ 2 ions in all constructs under physiological $[Ca^{2+}]_i$.

Discussion

Recent studies have highlighted a critical role for DOC2B as a high-affinity Ca^{2+} sensor in synaptic transmission. By interacting with membranes, SNARE proteins and additional factors, DOC2B enhances spontaneous and asynchronous neurotransmitter release. [1; 6; 23; 24; 25] Here, we structurally and biochemically analyzed the individual C_2 domains and the C2AB tandem to shed light on DOC2B's Ca^{2+}binding properties and the conformational and functional effects of Ca^{2+} on DOC2B.

C2A and C2B are functionally distinct despite the structural similarity – As may be expected from the high degree of conservation and from other C_2 domain structures, C2A and C2B are nearly structurally identical. Moreover, their respective Ca^{2+} coordination sites are highly similar in terms of the number of ligands and bond distances. However, we found that Ca^{2+} binding to C2A could not be detected up to $[Ca^{2+}]_{free}$ = 100 μM, while C2B possesses intrinsic affinity of ~10 μM (Figure 3D). The crystallographic studies also support these data, as 200 μM in the crystallization solution did not suffice for crystallizing C2A in a fully Ca^{2+}-loaded form, while for C2B, it did (Figure 1). These biochemical findings are supported by the live cell experiments that show that C2B functions physiologically as the primary sensor in a cellular system by demonstrating that C2B translocates to the PM of PC12 cells in response to physiological sub micro-molar $[Ca^{2+}]_i$ elevations while C2A required supra-physiological $[Ca^{2+}]_i$. This is consistent with previous work [34] in adipocytes which showed that deletion of C2B but not C2A eliminates the translocation ability of DOC2B. Intriguingly, despite the fact that C2B and C2AB bind Ca^{2+} in nearly identical fashion, the tandem C2AB translocated to the PM under two-fold lower Ca^{2+} concentrations and to a greater extent than C2B. This result suggests that C2A enhances DOC2B-PM interactions, probably due to low affinity interactions of C2A with the membrane. C2A probably does not serve as a primary sensor in C2AB or DOC2B as the Hill coefficients of these constructs resemble that of C2B, consistent with binding of ~ 2 ions to induce translocation. Taken together, these results suggest that under physiological conditions, the C2B functions as the primary Ca^{2+} sensor of DOC2B.

The C2AB tandem is highly flexible – We explored the structure of the tandem C_2 domains e.g. their relative orientation using SAXS, addressing how the tandem domains may behave in concert. The results show that the domains may undergo large conformational fluctuations in solution and that the

conformational equilibrium is not affected by Ca^{2+} binding. The domains are largely independently oriented in solution. These results are also consistent with site-directed spin labeling studies of syt 1 [35] that demonstrated flexibly linked non-interacting domains in the presence and absence of Ca^{2+}. Single molecule FRET studies of syt3 also showed that Ca^{2+} binding has no considerable effect on the FRET efficiency distribution. [20] However, in that case, the FRET efficiency distribution indicates that more molecules possess an elongated conformation rather than a compact conformation, while the D_{max} distribution derived from our SAXS experiments describes an opposite trend. The significance and explanation of this difference is not clear. Nonetheless, the marked flexibility of the C2AB tandem may underlie its ability to induce fusion of SNARE-containing liposomes and membrane curvature in a Ca^{2+}-dependent manner. [6; 7] as the domains were shown to undergo major reorientation upon SNARE binding to syt3 C2AB. [20]

Ca^{2+} dissociation precedes C2AB-membrane dissociation – Recently, stopped-flow experiments have demonstrated bi-phasic kinetics for C2AB-ULV dissociation. [24] The dissociation in these experiments was monitored by decrease in FRET between endogenous aromatic residues of C2AB and dansyl-PE labeling the ULVs. The fast phase kinetics correlates well with the rate constant we derived for Ca^{2+} dissociation from the C2AB-ULV complex. The changes in FRET upon Ca^{2+} dissociation before disassembly of the C2AB-ULV complex are not surprising, as Ca^{2+} affects the fluorescence intensity of endogenous C2B aromatic residues. Thus, we posit that with decreasing $[Ca^{2+}]_i$, DOC2B-Ca^{2+} dissociation occurs in two phases: first, Ca^{2+} dissociates from C2B with a time constant of about 27 ms (Figure 4B) and in turn, the C2AB-ULV complex dissociates with a time constant of 300 ms [24]. Such slow dissociation of the C2AB from ULV correlates with the time constants of asynchronous neurotransmitter release at the synapse[24] and with the contribution of DOC2B to asynchronous release phase. [24; 25]

A working model for DOC2B's role in membrane fusion – Collectively, our structural, physiological and biochemical analyses of DOC2B's C_2 domains suggest that despite their striking structural similarity, C2B functions as the primary Ca^{2+} sensor. Upon rise in $[Ca^{2+}]_i$, Ca^{2+} binding drives membrane association of DOC2B. After membrane association via C2B, C2A may bind Ca^{2+} in specific high $[Ca^{2+}]$ microdomains or may increase its affinity due to the vicinity of PLs head groups

as suggested for other C_2 domains. [8; 12] The finding that C2A can affect DOC2B interaction with the membrane is also supported from observations of $DOC2B^{D218,220N}$, a DOC2B with mutations in C2A, found to be constitutively associated with the PM. [1; 23] These previous data suggested that C2A serves as the primary DOC2B Ca^{2+} sensor. However, the current study clearly shows that C2A can boost DOC2B association with the PM but that C2B is the primary DOC2B Ca^{2+} sensor. It also reconciles previous work [34] in adipocytes which indicated that C2B of DOC2B is important for its translocation to the PM.

The crystal structures presented here suggest that H158 and F222, rather than N159, would mediate C2A membrane association (Figure 4B-C). Upon decrease in $[Ca^{2+}]_i$, Ca^{2+} first dissociates from DOC2B, driving its sequential dissociation from the membrane. The effect of Ca^{2+} may then be attributed to an electrostatic-switch mechanism as with other C_2 domains, [17; 18; 19] as it induces only minor changes in the inter- and intra-domain structures, if at all.

Materials and Methods

Expression and purification of C_2 proteins – The DNA constructs of C2A (encoding residues 125–255), C2B (encoding residues 265-412) and C2AB (encoding residues 125-412) of rat DOC2B (accession code NP_112404) were cloned into pRSFDuet-1 (Novagen) and expressed in *E. coli* Rosetta2 (DE3) competent cells (Novagen), as described. [36] An N-terminal 6xHis-tag, followed by TEV protease cleavage site and a short linker were added. Overexpressed proteins were purified on a Ni-NTA column, followed by TEV protease cleavage of the N-terminus. The reaction mixture was buffer exchanged to remove imidazole and loaded again on a Ni-NTA column. The unbound protein was collected and loaded onto a preparative size-exclusion column, (Superdex-75 for C2A, C2B or Superdex-200 (GE Healthcare) for C2AB), fractions were pooled, concentrated and frozen at -80° C.

Crystallization, data collection and structure determination – Purified C2A and C2B at a concentration of ~10 mg/mL were prepared in buffer composed of 200 mM NaCl, 0.2 mM $CaCl_2$ and 20 mM Tris-HCl (pH = 6.8). For C2A, 10 mM β-mercaptoethanol was an additional buffer component. Initial crystallization screens were performed at 19° C using the sitting drop vapor diffusion method. Initial crystals of C2A were obtained with 0.5 M $LiSO_4$, 25% PEG 3350 and 0.1 M

Tris-HCl (pH = 8.5). Crystals were optimized by lowering the $LiSO_4$ concentration to 0.1 M and the pH to 5.5, using a Na-citrate buffer instead of Tris. Initial crystals of C2B were obtained with 20% isopropanol, 20% PEG 4000 and 0.1 M Na-citrate (pH = 5.6). Crystals were optimized by modifying the isopropanol concentration to 22.5% and pH to 5.3. Crystals were cryoprotected in 60% reservoir solution, 25% ethylene glycol, 10% water and flash-frozen in cryo-loops. Data were collected from flash-frozen crystals cryocooled to 110° K at beamline ID14-1 of the European Synchrotron Radiation Facility (Grenoble, France).

Data were processed using HKL2000. [37] The initial model of C2A was obtained using molecular replacement with the program PHASER[38] in the PHENIX suite using a data set that diffracted to ~3 Å. [39] The coordinates of rabphilin-3A C2A (PDB 2CHD) were used as a search model. The initial model of C2B was obtained using molecular replacement with the coordinates of rabphilin-3A C2B (PDB 2CM6) as a search model. The models were refined by PHENIX[39] with multiple rounds of manual model building, performed using COOT. [40] Data and refinement statistics are summarized in table 1.

Molecular dynamics simulations of C2B – The simulation was performed using the C2B crystal structure coordinates obtained in this study. The two Ca^{2+} ions were removed from the structure to monitor the dynamics of the apo form of the protein. A molecular dynamics simulation was performed using the GROMACS 4.0 suite of software, [41] using the GROMACS 53a6 force field. [42] The protein was embedded in a dodecahedron box containing the SPC water molecules (35,394 molecules) that was extended to at least 15 Å between the protein's structure and the edge of the box. Assuming normal charge states of ionizable groups corresponding to pH 7, the net charge of DOC2B structure is +5e. Hence, 23 sodium and 28 chloride ions were added to the structure box at random positions, to neutralize the system at a physiological salt concentration of 100 mM. Prior to the dynamics trajectory, internal constraints were relaxed by energy minimization. Following this step, an MD equilibration run was performed under position restraints for 40 ps. Then, an unrestrained MD run was initiated for 8 ns. During the MD run, the LINCS algorithm[43] was used in order to constrain the lengths of all bonds; the water molecules were restrained using the SETTLE algorithm. The time step for the simulation was 2 fs. The simulation was run under NPT conditions, using the Berendsen

coupling algorithm to keep the temperature and pressure constant (P = 1 bar; τ_P= 0.5 ps; τ_T = 0.1 ps; T = 300 K). Van der Waals (VDW) forces were treated using a cut-off of 12 Å. Long-range electrostatic forces were treated using the PME method. The coordinates were saved every 1 ps. Cluster analysis was performed for the simulation of C2B by the command g_cluster of the GROMACS 4.0 package. The cluster analysis was performed using the Gromos algorithm on the entire protein with an RMSD cut-off value of 0.15 nm[44] and resulted in 35 clusters. The first cluster includes 16.9% of the structures, the second comprises 15.7% and the third only 11%. The first cluster, representing the most dominant structure during the simulation, was used as the final apo form for C2B.

SAXS Data Collection and Analysis – SAXS data were measured at beamline X33 of the Deutsches Elektronen Synchrotron (DESY), Hamburg, Germany. Data were collected with X-ray beam at wavelength λ=1.5 Å, and the distance from the sample to detector (PILATUS 1M, Dectris Ltd) was 2.7 meters, covering a scattering vector range ($q=4\pi\sin\theta/\lambda$) from 0.06 to 6 nm^{-1}. Eight frames of two-dimensional images were recorded for each buffer or sample, with an exposure time of 15 s for each frame. The 2D images were reduced to one-dimensional scattering profiles and the scattering of the buffer was subtracted from the sample profile using software on site. [45] C2AB in buffer containing 200 mM NaCl, 20 mM β-mercaptoethanol, 20 mM Tris-HCl at pH 6.8 and either 10 mM $CaCl_2$ or 10 mM EDTA was measured. To account for possible inter-particle effects, each sample was measured at four concentrations: 15, 10, 5 and 2 mg/mL. Due to small inter-particle effects, the lowest concentration curve was merged with a higher concentration curve at q ~ 0.2 $Å^{-1}$ to prevent distortion of the low-angle data while preserving high signal-to-noise ratio at the higher angles, which are far less sensitive to such effects. [46] The experimental radius of gyration (R_g) and the forward scattering intensity $I(0)$ were calculated from data at low q values in the range of $qR_g < 1.3$, using the Guinier approximation: $\ln I(q) \approx \ln(I(0)) - R_g^2 q^2/3$. The largest dimension of the molecule, D_{max}, and the Porod volume were calculated using GNOM. [47] For EOM analysis, [30] unstructured residues at the N and C – termini of C2A and C2B were truncated. RANCH[30] was used to generate a pool of 10,000 structures with random C2A-C2B linker and termini, which are stereochemically feasible. These pools were input into GAJOE[30] that selects an ensemble fitting the experimental data best using a genetic

algorithm: 50 ensembles of 20 orientations each were "crossed" and "mutated" for 1,000 generations and the process was repeated 50 times.

$^{45}Ca^{2+}$ equilibrium binding – The equilibrium binding of $^{45}Ca^{2+}$ to proteins was measured as the protein-bound radioactivity retained after ultrafiltration. [33; 48] Proteins were concentrated and decalcified by addition of 10 mM EDTA. [48] To remove EDTA, the protein preparations were washed with decalcified buffer using an Ultracel-3K (Millipore) concentrator in order to reach [EDTA] < 1 nM. [48] The assay medium (1.5 ml), containing 10 μM protein with 200 mM NaCl, 20 mM Tris-HCl at pH 7, was placed in the upper chamber of an Ultracel-3K concentrator and the assay was performed as previously outlined. [33; 48; 49] The $[Ca^{2+}]_{free}$ fraction was measured as *a/b*, where *a* represents the radioactivity of the ultrafiltate and *b* represents the radioactivity in the upper chamber; thus $[Ca^{2+}]_{free} = [Ca^{2+}]_{tot} \cdot (a/b)$. Bound Ca^{2+} is calculated as $[Ca^{2+}\text{- Protein}] = [Ca^{2+}]_{tot} - [Ca^{2+}]_{free}$ and binding stoichiometry as $[Ca^{2+}\text{-Protein}]/[\text{Protein}]$. The $^{45}Ca^{2+}$-titration curves were fit to Hill equation using Origin 7.0 software (OriginLab). $[Ca^{2+}]_{residual}$ of decalcified buffer was measured by fluo-3. [33]

Stopped-flow experiments – The stopped-flow assays were performed with a three-syringe/two mixer SFM-3 instrument (BioLogic, France) as described. [33; 36; 48; 49] The data were analyzed with Bio-Kine 32 V4.45 software (Bio-Logic). In the stopped-flow experiments, the Ca^{2+} dissociation from proteins was monitored with Quin-2, as described, [33; 36; 48; 49] by mixing 100 μl from each syringe. Syringe A contained 100 μl of 10 μM protein pre-equilibrated with 200 μM Ca^{2+}, in the presence or absence of 44 nM vesicles. Syringe B contained 500 μM Quin-2 in TK-buffer. The dead time is ~ 3.9 ms, allowing measurement of rate constants up to ~300 s^{-1}.

Liposome preparation – Protein-free liposomes composed of 45% PC (Avanti, 850457), 30% PE (Avanti, 850757) and 25% PS (Avanti, 840035) lipids were mixed, diluted in chloroform and immediately placed into a rotory-vaporator (Buch). Vesicles were then hydrated in a 20 mM Tris (pH=7; HCl), 200 mM NaCl containing buffer to a final concentration of 5.7 mg/ml, and heated to 65º C for 2 h. ULVs were obtained by probe sonication (Ultra-sonic liquid processor; Heat Systems Inc.). To remove excess MLVs, vesicles were centrifuged for 15 min at 15,000g. ULVs diameter measured 100 μm by dynamic light scattering.

Cell culture and transfection – Rat adrenal pheochromocytoma (PC12) cells were cultured in DMEM (Gibco) media supplemented with 10% horse serum, 5% fetal bovine serum, and 1% penicillin/streptomycin at 37°C and 5% CO_2. For experiments, cells were plated into 12 well plates containing 0.1% PDL coated coverslips. Transfections were performed using Lipofectamine 2000 (Invitrogen) according to the manufacturer's instructions. Cells were used 16-24h after transfection.

Combined Ca^{2+} measurements and DOC2B translocation in PC12 cells – Constructs encoding DOC2B domains C2A (residues 125–255), C2B (residues 265-412) and C2AB (residues 125-412), all fused to eGFP, were created by deletion of relevant coding regions from a DOC2B-eGFP (N2) plasmid[50] using a standard Quickchange mutagenesis protocol. PC12 cells overexpressing either the C2A, C2B, C2AB or the full length protein were pre-incubated with a serum-free medium (Opti-MEM; Gibco) for 2 h at 37º C. In the second hour of incubation, a mixture of 1:1 5 μM Fura-4F AM (Invitrogen) and Pluronic F-127 was added. The cells were then transferred to an inverted Olympus IX-70 microscope (Till Photonics) for simultaneous measurements of Ca^{2+} and translocation of the expressed protein. Timelapse imaging was performed with an Andor Ixon 887 EMCCD camera (Andor) controlled by METAFLUOR software (Universal Imaging). A set of three images at three wavelengths (200 ms exposure each) was taken at 1 Hz; 488 nm was used to view eGFP and 350 nm and 380 nm were used to excite Fura to deduce the $[Ca^{2+}]_i$ at each time point according to the dual excitation ratio-imaging technique.[51] During the experiments the cells were continually perfused with fresh bath solution (140 mM NaCl, 3 mM KCl, 5 mM $CaCl_2$, 10 mM HEPES and 2 mg/mL glucose; pH 7.2–7.4, 280–320 mOsmol/L). The first ~30 s of recording were used to establish $[Ca^{2+}]_i$ basal levels. Then, the cells were exposed to several (2-5) repetitive stimuli by a 100 mM KCl solution (40 mM NaCl, 100 mM KCl, 10 mM $CaCl_2$, 10 mM HEPES and 2 mg/mL glucose; pH 7.2–7.4, 280–320 mOsmol/L), each lasting ~ 10 s. Applications were performed locally through a four-barrel-like pipette and the KCl solution was replaced with the bath solution immediately after each application. The interval between KCl applications was 1-2 min to allow $[Ca^{2+}]_i$ decline back to baseline. Data were analyzed using the MetaFluor analyst software. $[Ca^{2+}]_i$ values at each time point were deduced from the Grynkiewicz equation, [51] based on the fluorescence values received from the images taken at 350 and 380 nm as previously described, [23] and binned every 25 nM. Calibration of free $[Ca^{2+}]_i$

concentrations and the calculations of Ca^{2+} parameters required for translocation were conducted as previously described [23]. Translocation of eGFP labeled peptides was defined as the fluorescence value at the plasma membrane divided by the fluorescence in the center of the cell. [23] Then, peptides translocation values were drawn as a function of log($[Ca^{2+}]_i$) and data were fit to the Hill equation using the Origin 7.0 software (OriginLab). In the case of the C2A construct, a simple high K^+ stimulation did not elicit plasma-membrane translocation, and therefore 10 μM Ionomycin (Sigma) was added to a bath solution containing 135 mM NaCl, 3 mM KCl, 10 mM $CaCl_2$, 10 mM HEPES and 2 mg/mL glucose (pH 7.2–7.4, 280–320 mOsmol/L) to reach higher, non-physiological, Ca^{2+} concentrations. [52; 53]

Accession numbers Crystallographic data and coordinates have been deposited in the PDB under the codes 4LCV (C2A) and 4LDC (C2B).

Acknowledgments We thank the staffs of ID14-1, ID-23-1 and ID-23-2 at the ESRF for assistance with diffraction experimentation, the staff of X33 at DESY for assistance with SAXS experimentation, and Prof. Rimona Margalit and Dr. Ilia Rivkin for assistance with liposome preparation. This work was supported, in part, by Israel Science Foundation Grants 1211/07 and 730/11 and a German-Israeli Foundation Grant 1125-145.1/2010 to UA. JAH was funded by a DIP-DFG grant. This work was partially funded by the Israeli Ministry of Health Grant 2010-3-6266, the USA-Israel Binational Foundation Research Grant # 2009-334, Israel Science Foundation Grant # 23/10 to DK. MG was supported by a PhD fellowship from the Clore Scholars Program of the Clore Israel Foundation. The support of the Bernstein Foundation is highly appreciated.

References

1. Friedrich, R., Groffen, A. J., Connell, E., van Weering, J. R., Gutman, O., Henis, Y. I., Davletov, B. & Ashery, U. (2008). DOC2B acts as a calcium switch and enhances vesicle fusion. *J Neurosci* **28**, 6794-806.

2. Xue, M., Giagtzoglou, N. & Bellen, H. J. (2011). Dueling Ca^{2+} sensors in neurotransmitter release. *Cell* **147**, 491-3.

3. Pang, Z. P. & Sudhof, T. C. (2010). Cell biology of Ca^{2+}-triggered exocytosis. *Curr Opin Cell Biol* **22**, 496-505.

4. Nalefski, E. A. & Falke, J. J. (1996). The C_2 domain calcium-binding motif: structural and functional diversity. *Protein Sci* **5**, 2375-90.

5. Martens, S. & McMahon, H. T. (2012). C_2 domains and membrane fusion. *Curr Top Membr* **68**, 141-59.

6. Groffen, A. J., Martens, S., Diez Arazola, R., Cornelisse, L. N., Lozovaya, N., de Jong, A. P., Goriounova, N. A., Habets, R. L., Takai, Y., Borst, J. G., Brose, N., McMahon, H. T. & Verhage, M. (2010). Doc2b is a high-affinity Ca^{2+} sensor for spontaneous neurotransmitter release. *Science* **327**, 1614-8.

7. Yu, H., Rathore, S. S., Davis, E. M., Ouyang, Y. & Shen, J. (2013). Doc2b promotes GLUT4 exocytosis by activating the SNARE-mediated fusion reaction in a calcium- and membrane bending-dependent manner. *Mol Biol Cell*.

8. van den Bogaart, G., Meyenberg, K., Diederichsen, U. & Jahn, R. (2012). Phosphatidylinositol 4,5-bisphosphate increases Ca^{2+} affinity of synaptotagmin-1 by 40-fold. *J Biol Chem* **287**, 16447-53.

9. Lynch, K. L., Gerona, R. R., Larsen, E. C., Marcia, R. F., Mitchell, J. C. & Martin, T. F. (2007). Synaptotagmin C2A loop 2 mediates Ca^{2+}-dependent SNARE interactions essential for Ca^{2+}-triggered vesicle exocytosis. *Mol Biol Cell* **18**, 4957-68.

10. Hui, E., Bai, J. & Chapman, E. R. (2006). Ca^{2+}-triggered simultaneous membrane penetration of the tandem C_2-domains of synaptotagmin I. *Biophys J* **91**, 1767-77.

11. Popoli, M., Venegoni, A., Buffa, L. & Racagni, G. (1997). Ca^{2+}/phospholipid-binding and syntaxin-binding of native synaptotagmin I. *Life Sci* **61**, 711-21.

12. Radhakrishnan, A., Stein, A., Jahn, R. & Fasshauer, D. (2009). The Ca^{2+} affinity of synaptotagmin 1 is markedly increased by a specific interaction of its C2B domain with phosphatidylinositol 4,5-bisphosphate. *J Biol Chem* **284**, 25749-60.

13. Corbin, J. A., Evans, J. H., Landgraf, K. E. & Falke, J. J. (2007). Mechanism of specific membrane targeting by C2 domains: localized pools of target lipids enhance Ca^{2+} affinity. *Biochemistry* **46**, 4322-36.

14. Coudevylle, N., Montaville, P., Leonov, A., Zweckstetter, M. & Becker, S. (2008). Structural determinants for Ca^{2+} and phosphatidylinositol 4,5-bisphosphate binding by the C2A domain of rabphilin-3A. *J Biol Chem* **283**, 35918-28.

15. Montaville, P., Coudevylle, N., Radhakrishnan, A., Leonov, A., Zweckstetter, M. & Becker, S. (2008). The PIP2 binding mode of the C_2 domains of rabphilin-3A. *Protein Sci* **17**, 1025-34.

16. Montaville, P., Schlicker, C., Leonov, A., Zweckstetter, M., Sheldrick, G. M. & Becker, S. (2007). The C2A-C2B linker defines the high affinity Ca^{2+} binding mode of rabphilin-3A. *J Biol Chem* **282**, 5015-25.

17. Shao, X., Fernandez, I., Sudhof, T. C. & Rizo, J. (1998). Solution structures of the Ca^{2+}-free and Ca^{2+}-bound C2A domain of synaptotagmin I: does Ca^{2+} induce a conformational change? *Biochemistry* **37**, 16106-15.

18. Murray, D. & Honig, B. (2002). Electrostatic control of the membrane targeting of C_2 domains. *Mol Cell* **9**, 145-54.

19. Rizo, J. & Sudhof, T. C. (1998). C_2-domains, structure and function of a universal Ca^{2+}-binding domain. *J Biol Chem* **273**, 15879-82.

20. Vrljic, M., Strop, P., Ernst, J. A., Sutton, R. B., Chu, S. & Brunger, A. T. (2010). Molecular mechanism of the synaptotagmin-SNARE interaction in Ca^{2+}-triggered vesicle fusion. *Nat Struct Mol Biol* **17**, 325-31.

21. Choi, U. B., Strop, P., Vrljic, M., Chu, S., Brunger, A. T. & Weninger, K. R. (2010). Single-molecule FRET-derived model of the synaptotagmin 1-SNARE fusion complex. *Nat Struct Mol Biol* **17**, 318-24.

22. Hui, E., Bai, J., Wang, P., Sugimori, M., Llinas, R. R. & Chapman, E. R. (2005). Three distinct kinetic groupings of the synaptotagmin family: candidate sensors for rapid and delayed exocytosis. *Proc Natl Acad Sci U S A* **102**, 5210-4.

23. Groffen, A. J., Friedrich, R., Brian, E. C., Ashery, U. & Verhage, M. (2006). DOC2A and DOC2B are sensors for neuronal activity with unique calcium-dependent and kinetic properties. *J Neurochem* **97**, 818-33.

24. Yao, J., Gaffaney, J. D., Kwon, S. E. & Chapman, E. R. (2011). Doc2 is a Ca^{2+} sensor required for asynchronous neurotransmitter release. *Cell* **147**, 666-77.

25. Lavi, A., Sheinin, A., Shapira, R., Zelmanoff, D. & Ashery, U. (2013). DOC2B and Munc13-1 Differentially Regulate Neuronal Network Activity. *Cereb Cortex*.

26. Fernandez, I., Arac, D., Ubach, J., Gerber, S. H., Shin, O., Gao, Y., Anderson, R. G., Sudhof, T. C. & Rizo, J. (2001). Three-dimensional structure of the synaptotagmin 1 C2B-domain: synaptotagmin 1 as a phospholipid binding machine. *Neuron* **32**, 1057-69.

27. Ubach, J., Zhang, X., Shao, X., Sudhof, T. C. & Rizo, J. (1998). Ca^{2+} binding to synaptotagmin: how many Ca^{2+} ions bind to the tip of a C_2-domain? *Embo J* **17**, 3921-30.

28. Ubach, J., Garcia, J., Nittler, M. P., Sudhof, T. C. & Rizo, J. (1999). Structure of the Janus-faced C2B domain of rabphilin. *Nat Cell Biol* **1**, 106-12.

29. Petoukhov, M. V. & Svergun, D. I. (2005). Global rigid body modeling of macromolecular complexes against small-angle scattering data. *Biophys J* **89**, 1237-50.

30. Bernado, P., Mylonas, E., Petoukhov, M. V., Blackledge, M. & Svergun, D. I. (2007). Structural characterization of flexible proteins using small-angle X-ray scattering. *J Am Chem Soc* **129**, 5656-64.

31. Chapman, E. R. & Davis, A. F. (1998). Direct interaction of a Ca^{2+}-binding loop of synaptotagmin with lipid bilayers. *J Biol Chem* **273**, 13995-4001.

32. Bai, J., Tucker, W. C. & Chapman, E. R. (2004). PIP_2 increases the speed of response of synaptotagmin and steers its membrane-penetration activity toward the plasma membrane. *Nat Struct Mol Biol* **11**, 36-44.

33. Boyman, L., Mikhasenko, H., Hiller, R. & Khananshvili, D. (2009). Kinetic and equilibrium properties of regulatory calcium sensors of NCX1 protein. *J Biol Chem* **284**, 6185-93.

34. Fukuda, N., Emoto, M., Nakamori, Y., Taguchi, A., Miyamoto, S., Uraki, S., Oka, Y. & Tanizawa, Y. (2009). DOC2B: a novel syntaxin-4 binding protein mediating insulin-regulated GLUT4 vesicle fusion in adipocytes. *Diabetes* **58**, 377-84.

35. Herrick, D. Z., Kuo, W., Huang, H., Schwieters, C. D., Ellena, J. F. & Cafiso, D. S. (2009). Solution and membrane-bound conformations of the tandem C2A and C2B domains of synaptotagmin 1: Evidence for bilayer bridging. *J Mol Biol* **390**, 913-23.

36. Giladi, M., Sasson, Y., Fang, X., Hiller, R., Buki, T., Wang, Y. X., Hirsch, J. A. & Khananshvili, D. (2012). A common Ca^{2+}-driven interdomain module governs eukaryotic NCX regulation. *PLoS One* **7**, e39985.

37. Otwinowski, Z. & Minor, W. (1997). Processing of X-ray Diffraction Data Collected in Oscillation Mode. *Methods in Enzymology* **276**, 307-326.

38. McCoy, A. J., Grosse-Kunstleve, R. W., Adams, P. D., Winn, M. D., Storoni, L. C. & Read, R. J. (2007). Phaser crystallographic software. *J Appl Crystallogr* **40**, 658-674.

39. Adams, P. D., Afonine, P. V., Bunkoczi, G., Chen, V. B., Davis, I. W., Echols, N., Headd, J. J., Hung, L. W., Kapral, G. J., Grosse-Kunstleve, R. W., McCoy, A. J., Moriarty, N. W., Oeffner, R., Read, R. J., Richardson, D. C., Richardson, J. S., Terwilliger, T. C. & Zwart, P. H. (2010). PHENIX: a comprehensive Python-based system for macromolecular structure solution. *Acta Crystallogr D Biol Crystallogr* **66**, 213-21.

40. Emsley, P. & Cowtan, K. (2004). Coot: model-building tools for molecular graphics. *Acta Crystallogr D Biol Crystallogr* **60**, 2126-32.

41. Van Der Spoel, D., Lindahl, E., Hess, B., Groenhof, G., Mark, A. E. & Berendsen, H. J. (2005). GROMACS: fast, flexible, and free. *J Comput Chem* **26**, 1701-18.

42. Oostenbrink, C., Villa, A., Mark, A. E. & van Gunsteren, W. F. (2004). A biomolecular force field based on the free enthalpy of hydration and solvation: the GROMOS force-field parameter sets 53A5 and 53A6. *J Comput Chem* **25**, 1656-76.

43. Hess, B., Bekker, H., Berendsen, H. J. C. & Fraaije, J. G. E. M. (1997). LINCS: A linear constraint solver for molecular simulations. *J Comput Chem* **18**, 1463-1472.

44. Daura, X., van Gunsteren, W. F. & Mark, A. E. (1999). Folding-unfolding thermodynamics of a beta-heptapeptide from equilibrium simulations. *Proteins* **34**, 269-80.

45. Franke, D., Kikhney, A. G. & Svergun, D. I. (2012). Automated acquisition and analysis of small angle X-ray scattering data. *Nucl Instrum Meth A* **689**, 52-59.

46. Koch, M. H., Vachette, P. & Svergun, D. I. (2003). Small-angle scattering: a view on the properties, structures and structural changes of biological macromolecules in solution. *Q Rev Biophys* **36**, 147-227.

47. Svergun, D. I. (1992). Determination of the regularization parameter in indirect-transform methods using perceptual criteria. *J Appl Crystallogr* **25**, 495-503.

48. Giladi, M., Bohbot, H., Buki, T., Schulze, D. H., Hiller, R. & Khananshvili, D. (2012). Dynamic features of allosteric Ca^{2+} sensor in tissue-specific NCX variants. *Cell Calcium* **51**, 478-85.

49. Giladi, M., Boyman, L., Mikhasenko, H., Hiller, R. & Khananshvili, D. (2010). Essential role of the CBD1-CBD2 linker in slow dissociation of Ca^{2+} from the regulatory two-domain tandem of NCX1. *J Biol Chem* **285**, 28117-25.

50. Groffen, A. J., Brian, E. C., Dudok, J. J., Kampmeijer, J., Toonen, R. F. & Verhage, M. (2004). Ca^{2+}-induced recruitment of the secretory vesicle protein DOC2B to the target membrane. *J Biol Chem* **279**, 23740-7.

51. Grynkiewicz, G., Poenie, M. & Tsien, R. Y. (1985). A new generation of Ca^{2+} indicators with greatly improved fluorescence properties. *J Biol Chem* **260**, 3440-50.

52. Liu, C. & Hermann, T. E. (1978). Characterization of ionomycin as a calcium ionophore. *J Biol Chem* **253**, 5892-4.

53. Perlman, R. L., Cossi, A. F. & Role, L. W. (1980). Mechanisms of ionophore-induced catecholamine secretion. *J Pharmacol Exp Ther* **213**, 241-6.

54. Baker, N. A., Sept, D., Joseph, S., Holst, M. J. & McCammon, J. A. (2001). Electrostatics of nanosystems: application to microtubules and the ribosome. *Proc Natl Acad Sci U S A* **98**, 10037-41.

Figure legends

Figure 1. Structure of DOC2B C_2 domains. (A) Crystal structures of C2A in the apo- and Ca^{2+} bound forms, C2B in the bound form and a structural model of C2B in the apo form, in cartoon representation. C2A and C2B are colored orange and red, respectively. Green and cyan spheres depict Ca^{2+} ions and water molecules, respectively. (B) Electrostatic potentials of C2A and C2B in the apo- and Ca^{2+} bound forms. The bar indicates potentials ranging from -5 (red) to +5 (blue) kT/e. The electrostatic potentials were calculated using APBS and are depicted on the accessible surface. [54]

Figure 2. SAXS analysis of C2AB reveals high flexibility for the tandem C2AB. Experimental SAXS data were fit using SASREF (A) or EOM (B). (C) Random R_g and D_{max} pools and EOM selected ensembles for C2AB, as indicated. (D) Normalized pair distance distribution functions (PDDF) of C2AB. (E) Representative orientations of C2AB, found in the EOM analysis.

Figure 3. Similar Ca^{2+} binding sites but different equilibrium binding for C2A and C2B. Ca^{2+}binding sites of the C2A (A) Ca^{2+} bound and (B) apo forms (orange) and (C) C2B Ca^{2+} bound form crystal structures (red). Residues coordinating Ca^{2+} are depicted as sticks. (D) $^{45}Ca^{2+}$ titration curves of isolated C2A (black), C2B (red) and C2AB (blue). Each titration was repeated twice and fit to the Hill equation.

Figure 4. Effect of Ca^{2+} binding to C2A on B-factors. (A) Average B-factor for each residue in the apo (black) and Ca^{2+} bound (red) forms. (B) The apo (left) and Ca^{2+}-bound (right) C2A colored according to the respective B-factors. Residues implicated in membrane penetration are shown as sticks. (C) Superposition of the C2A apo (left) and Ca^{2+} bound (right) forms of DOC2B (orange) and syt1 (cyan, PDB 1RSY and 1BYN, respectively). Residues implicated in membrane penetration are shown as sticks. Spheres indicate Ca^{2+} ions.

Figure 5. Ca^{2+} dissociation kinetics of C2AB. (A) Representative traces of Ca^{2+} dissociation kinetics from C2AB in the absence and presence of ULVs, as indicated, were fit to a single exponential curve

with k_{off} = 314.9 ± 5.7 s^{-1} and k_{off} = 35.1 ± 0.2 s^{-1}, respectively. (B) Kinetic scheme of Ca^{2+} dissociation from C2AB. Two Ca^{2+} ions dissociate from C2B upon addition of Quin-2 in a monophasic fashion with k_{off} = 264.5 ± 17.7 s^{-1}in the absence of ULVs. In the presence of ULVs, two Ca^{2+} ions dissociate from C2B in a monophasic fashion with k_{off} = 36.5 ± 0.7 s^{-1}. Following Ca^{2+} dissociation, the C2AB-ULV complex dissociates with k_{off} = 3.3 ± 0.5 s^{-1} [24]. Occupied Ca^{2+} sites are denoted by filled circles, whereas open circles represent empty sites.

Figure 6. Ca^{2+}-dependent translocation of DOC2B constructs suggests that C2B is the primary Ca^{2+} sensor in cells. (A) Representative images of DOC2B-GFP and its fragments expressed in PC12 cells before and after KCl application or after application **of** Ca^{2+} ionophore (C2A). (B) Quantification of Ca^{2+} dependent translocation for full length DOC2B, C2AB and C2B, achieved by simultaneously monitoring intracellular Ca^{2+} levels and translocation status (left). Translocation was defined as PM/cytosol fluorescence ratio, and data is presented as mean ± SE. Normalized translocation values showed as a function of intracellular Ca^{2+} concentration (right). (C) EC_{50} (μM) and nH values of full length DOC2B, C2AB and C2B calculated from a dose-response fit of the data presented in panel B.

Table 1 - Crystallographic statistics

Data statistics	**C2A**	**C2B**
Wavelength (Å)	0.934 Å	0.934 Å
Space group	$P2_1$	C2
Unit cell parameters (Å)	*a* = 43.6, *b* = 95.2, *c* = 67.8 β = 99.9º	*a* = 90.8, *b* = 40.1, *c* = 36.9 β = 105.5º
Total reflections	133180	98104
Unique reflections	34604	33561
Completeness (%)	94.6 (73.6)	92.2 (29.4)
R_{merge} (%)	7.2	2.7
I/σ	17.2 (2.1)	36.2 (8.2)
Resolution range (Å)	50.0 – 2.0	50.0–1.24
X-ray source	ESRF beamline ID14-1	ESRF beamline ID14-1
Refinement statistics		
No. of reflections (working/test)	34576/1727	33558/1683
d_{min} (Å)	2.00	1.26
R_{work}/R_{free} (%)	18.7/23.2	12.7/14.4
RMS deviation from ideality:		
Bond lengths	0.005	0.006
Bond angles	0.95	1.11
B factors ($Å^2$) (rms deviation of bonded atoms-main/side chain)	3.43/4.65	0.86/2.34
Average B factor protein atoms/solvent ($Å^2$)	38.3/40	7.2/22.8
Ramachadran favored/outliers (%)	96/0.6	95/0
No. of atoms protein/ligands/water	3943/39/261	2356/20/214

* Statistics for the highest-resolution shell are shown in parentheses.

Table 2 - SAXS data collection and scattering-derived parameters

Sample	**C2AB**	
Ligand	10 mM Ca^{2+}	10 mM EDTA
Data collection parameters		
Beamline	DESY X33	
Beam geometry (mm^2)	2 x 0.6	
Wavelength (Å)	1.5	
q range ($Å^{-1}$)	0.006-0.6	
Exposure time per frame (seconds)[1]	15	
Concentration range (mg/ml)	2-15	
Temperature (°C)	5	
Structural parameters		
I(0) (from Guinier)[2]	30.3 ± 0.1	28.7 ± 0.1
R_g (Å) (from Guinier)[2]	26.0 ± 0.2	25.2 ± 0.2
D_{max} (Å)[3]	83 ± 8	80 ± 8
χ^2 (SASREF)	1.12	1.52
χ^2 (EOM)	0.75	0.66
Porod volume [from *P(r)*] (10^3 $Å^3$)	41.7	41.5
Software employed		
Primary data reduction	AUTOMAR	
Data processing	PRIMUS	
Modelling	EOM	

[1] Eight frames were measured for each sample. [2] ± S.E. [3] ± 10% (estimated range).

Figure 1

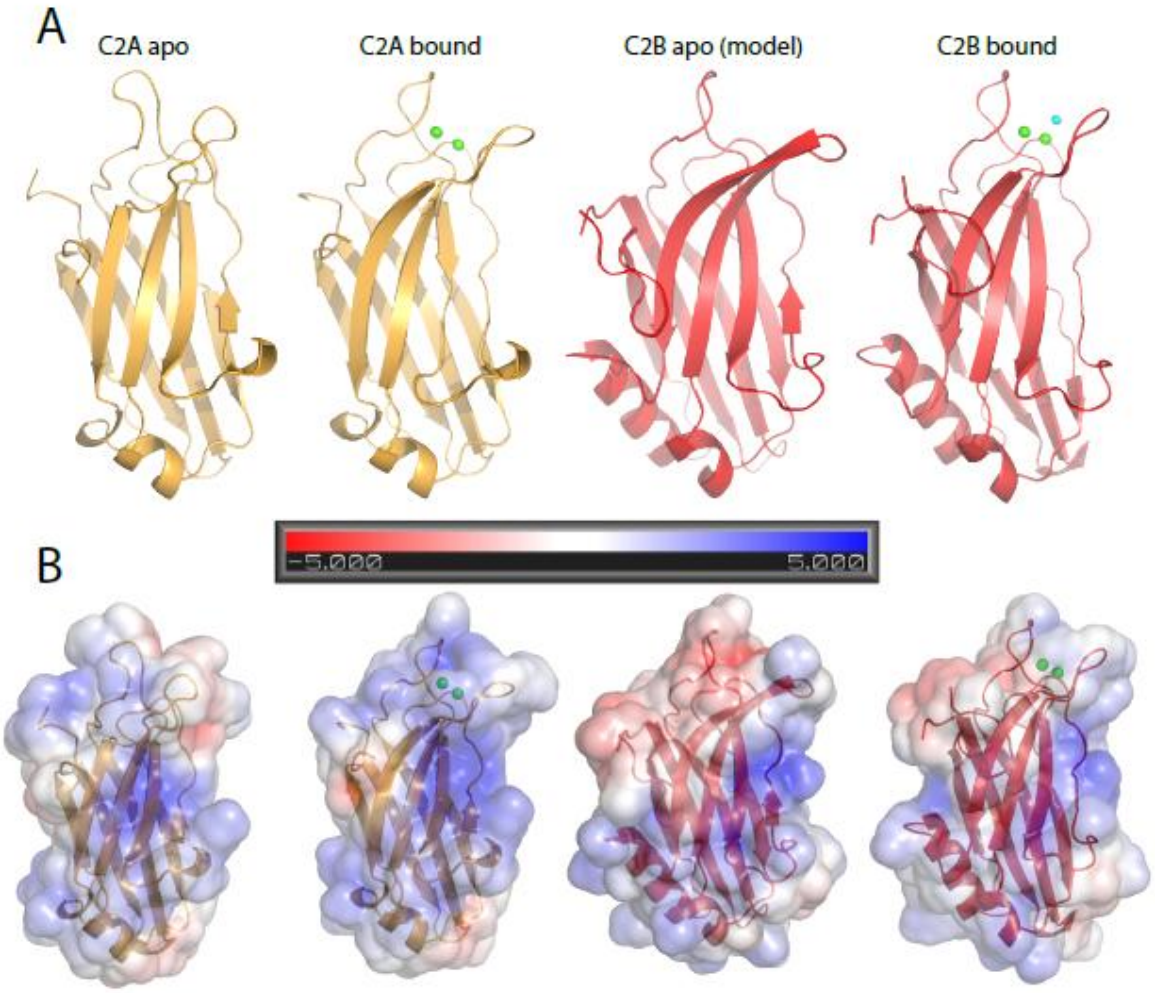

Figure 2

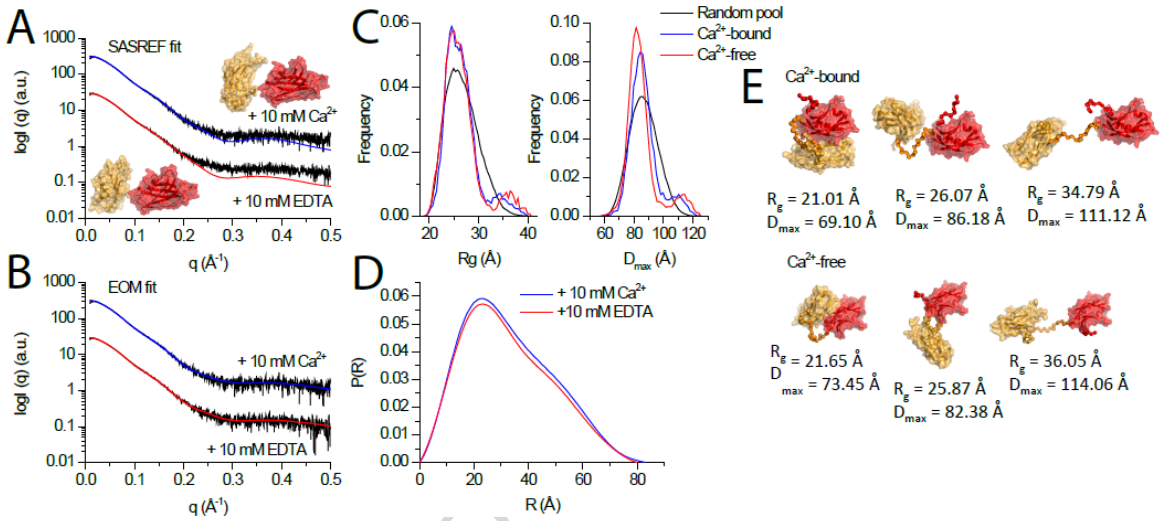

Figure 3

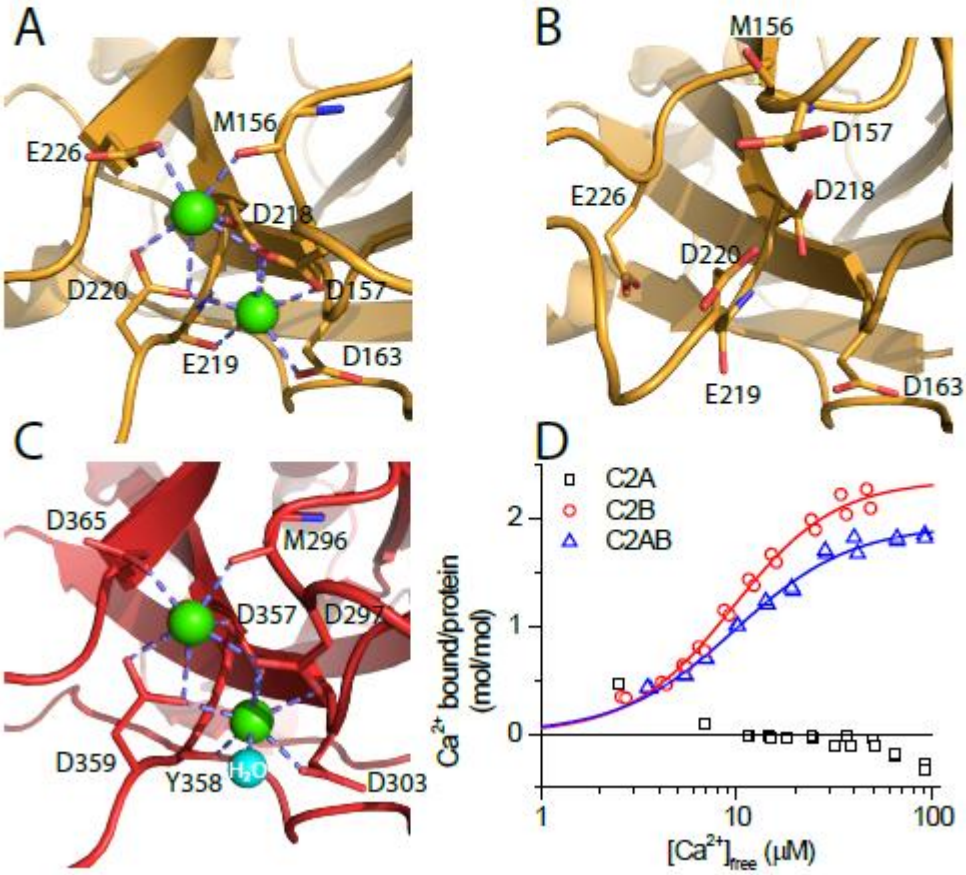

Figure 4

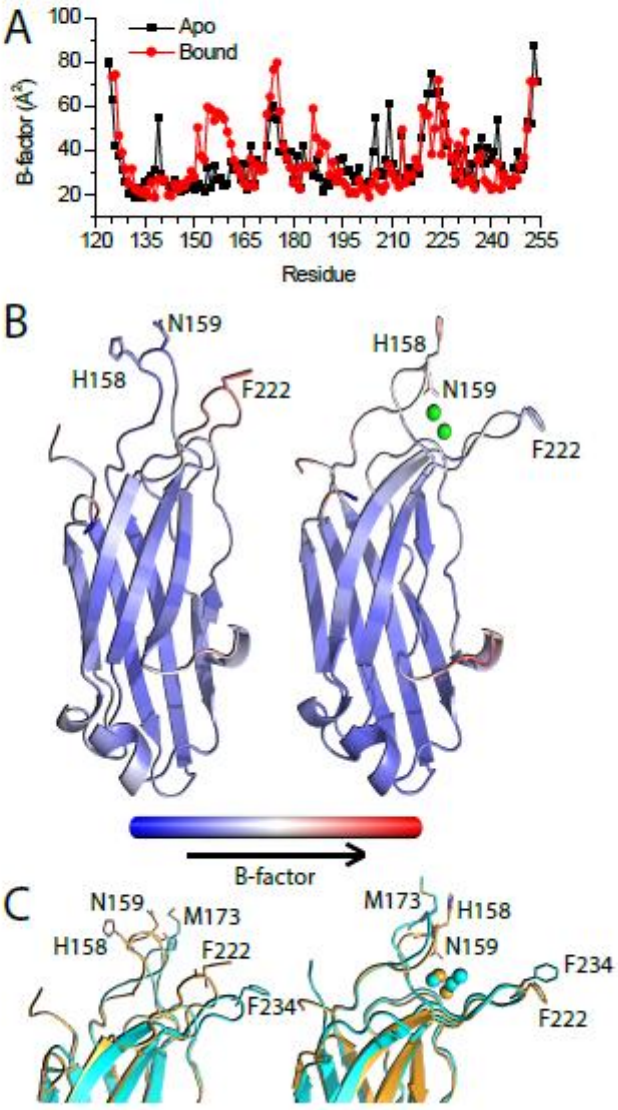

Figure 5

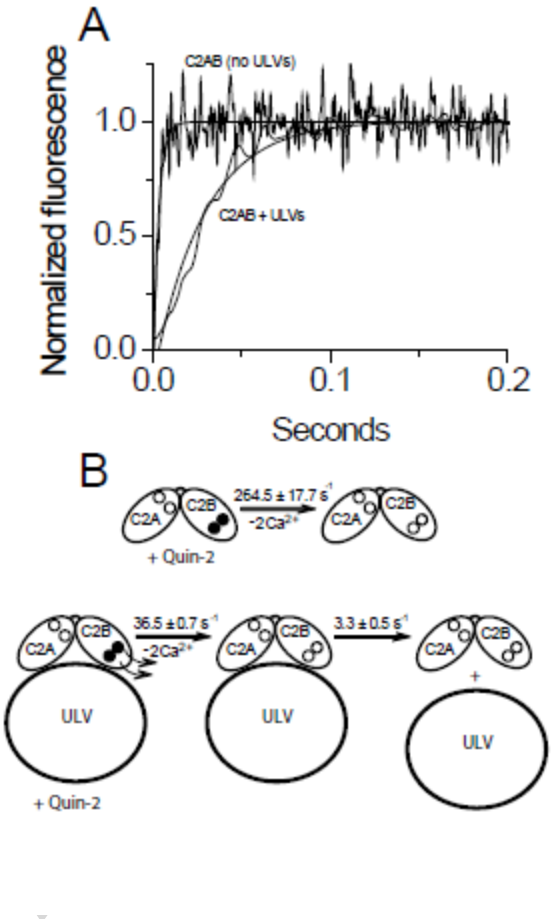

Figure 6

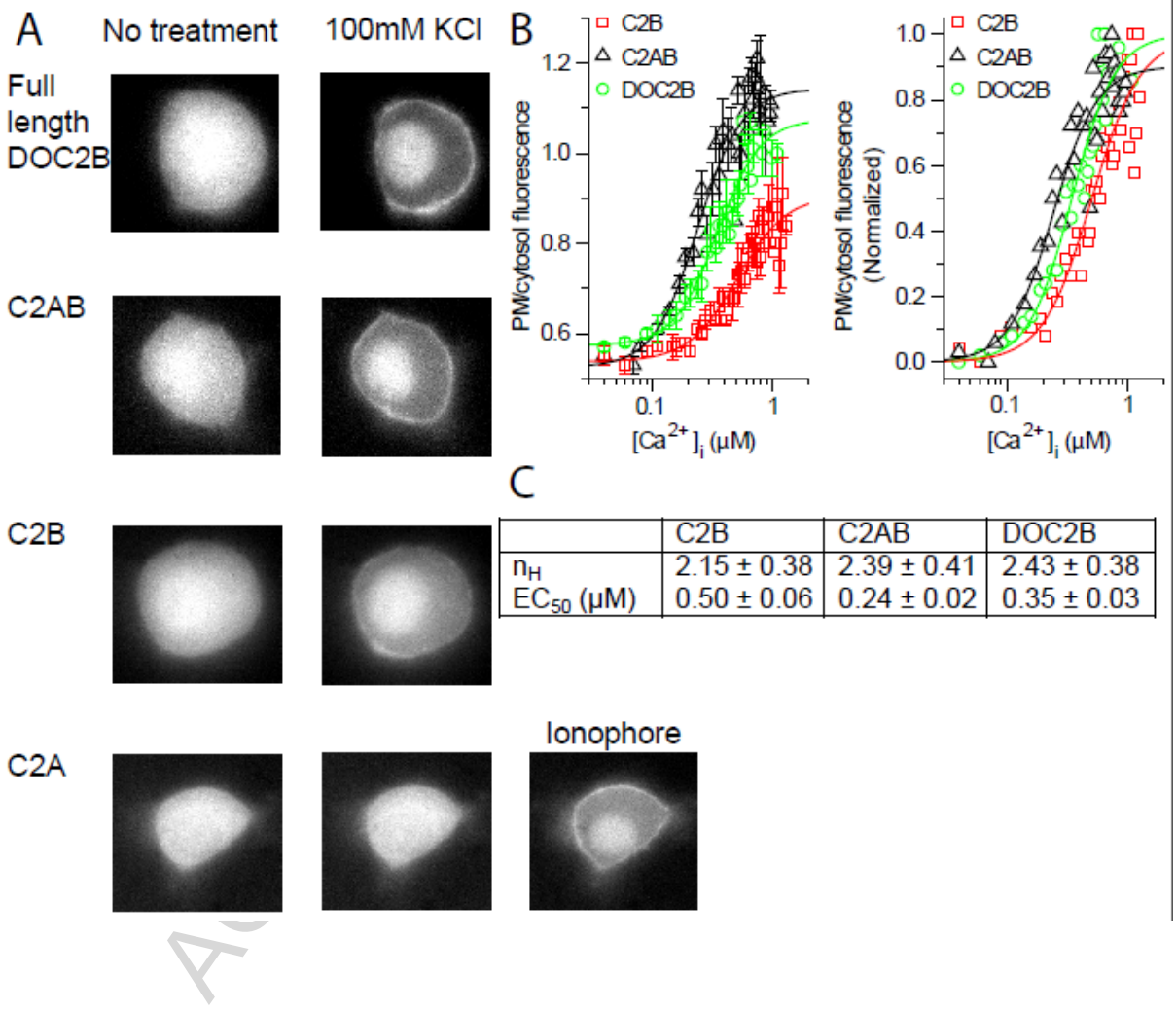

	C2B	C2AB	DOC2B
n_H	2.15 ± 0.38	2.39 ± 0.41	2.43 ± 0.38
EC_{50} (μM)	0.50 ± 0.06	0.24 ± 0.02	0.35 ± 0.03

Graphical Abstract

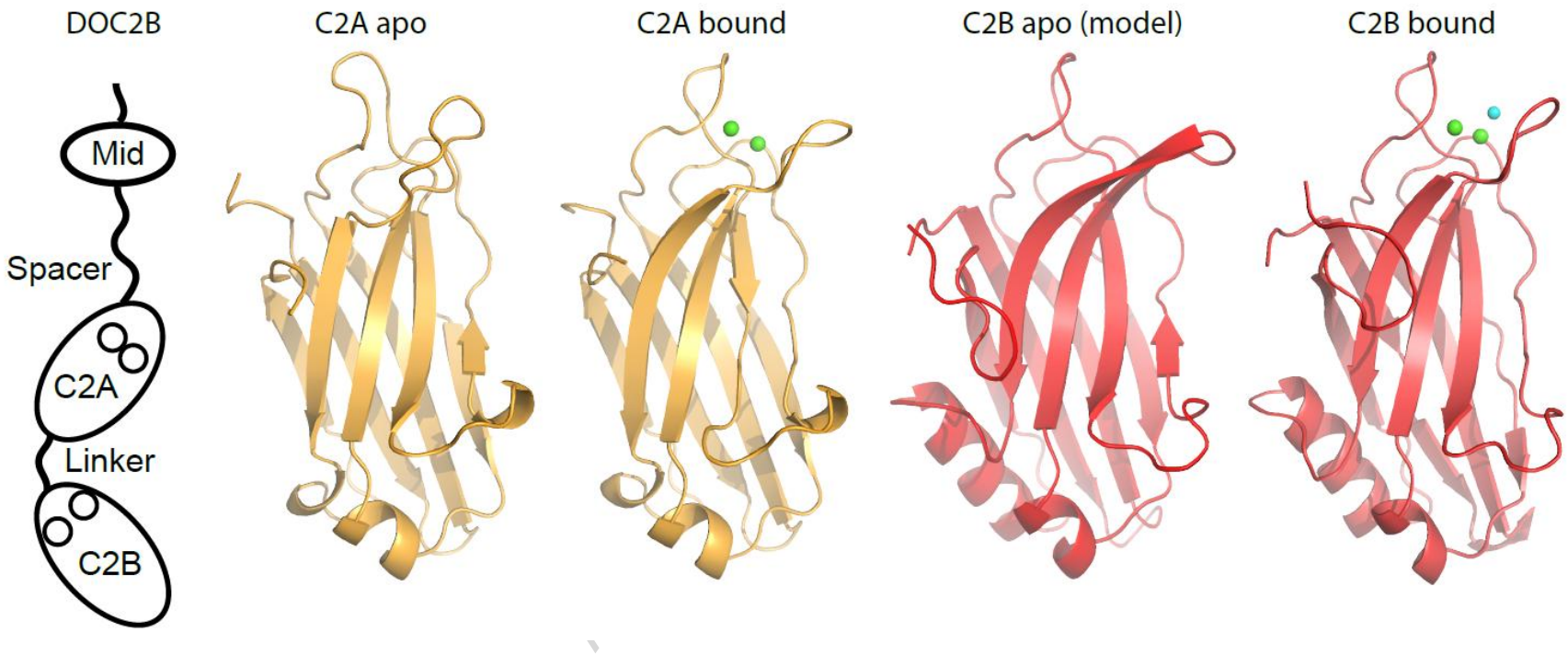

Highlights

- DOC2B is a Ca^{2+} sensor for spontaneous and asynchronous neurotransmitter release
- Crystal structures of the individual C2 domains and solution structure of the tandem
- C2B is the primary Ca2+ sensor and is necessary for membrane translocation
- C2A enhances membrane translocation